Measurement of charmless B decays to ηK^* and $\eta\rho$

C. H. Wang,[29] K. Abe,[10] I. Adachi,[10] H. Aihara,[52] D. Anipko,[1] T. Aushev,[16,22] A. M. Bakich,[47] E. Barberio,[25] A. Bay,[22] K. Belous,[15] U. Bitenc,[17] S. Blyth,[28] A. Bondar,[1] A. Bozek,[31] M. Bračko,[10,17,24] P. Chang,[30] Y. Chao,[30] A. Chen,[28] W. T. Chen,[28] B. G. Cheon,[8] R. Chistov,[16] Y. Choi,[46] Y. K. Choi,[46] S. Cole,[47] J. Dalseno,[25] A. Drutskoy,[3] S. Eidelman,[1] S. Fratina,[17] N. Gabyshev,[1] A. Garmash,[40] T. Gershon,[10] G. Gokhroo,[48] B. Golob,[17,23] H. Ha,[19] J. Haba,[10] T. Hara,[36] K. Hayasaka,[26] M. Hazumi,[10] D. Heffernan,[36] T. Hokuue,[26] Y. Hoshi,[50] W.-S. Hou,[30] T. Iijima,[26] K. Ikado,[26] A. Imoto,[27] K. Inami,[26] A. Ishikawa,[52] H. Ishino,[53] R. Itoh,[10] M. Iwasaki,[52] Y. Iwasaki,[10] H. Kaji,[26] J. H. Kang,[59] P. Kapusta,[31] N. Katayama,[10] H. R. Khan,[53] H. Kichimi,[10] Y. J. Kim,[6] K. Kinoshita,[3] R. Kulasiri,[3] R. Kumar,[37] C. C. Kuo,[28] Y.-J. Kwon,[59] G. Leder,[14] M. J. Lee,[44] S. E. Lee,[44] T. Lesiak,[31] S.-W. Lin,[30] D. Liventsev,[16] J. MacNaughton,[14] T. Matsumoto,[54] A. Matyja,[31] S. McOnie,[47] H. Miyake,[36] H. Miyata,[33] R. Mizuk,[16] E. Nakano,[35] M. Nakao,[10] Z. Natkaniec,[31] S. Nishida,[10] O. Nitoh,[55] S. Ogawa,[49] T. Ohshima,[26] S. Okuno,[18] Y. Onuki,[41] H. Ozaki,[10] P. Pakhlov,[16] G. Pakhlova,[16] H. Park,[21] K. S. Park,[46] R. Pestotnik,[17] L. E. Piilonen,[58] Y. Sakai,[10] N. Satoyama,[45] O. Schneider,[22] J. Schümann,[29] K. Senyo,[26] M. E. Sevior,[25] M. Shapkin,[15] H. Shibuya,[49] J. B. Singh,[37] A. Sokolov,[15] A. Somov,[3] N. Soni,[37] S. Stanič,[34] M. Starič,[17] H. Stoeck,[47] S. Y. Suzuki,[10] K. Tamai,[10] M. Tanaka,[10] G. N. Taylor,[25] Y. Teramoto,[35] X. C. Tian,[38] I. Tikhomirov,[16] T. Tsuboyama,[10] T. Tsukamoto,[10] S. Uehara,[10] T. Uglov,[16] K. Ueno,[30] P. Urquijo,[25] Y. Usov,[1] G. Varner,[9] S. Villa,[22] M.-Z. Wang,[30] Y. Watanabe,[53] E. Won,[19] Q. L. Xie,[13] A. Yamaguchi,[51] Y. Yamashita,[32] C. C. Zhang,[13] Z. P. Zhang,[43] V. Zhilich,[1] and A. Zupanc[17]

(Belle Collaboration)

[1]*Budker Institute of Nuclear Physics, Novosibirsk*
[2]*Chiba University, Chiba*
[3]*University of Cincinnati, Cincinnati, Ohio 45221*
[4]*Department of Physics, Fu Jen Catholic University, Taipei*
[5]*Justus-Liebig-Universität Gießen, Gießen*
[6]*The Graduate University for Advanced Studies, Hayama*
[7]*Gyeongsang National University, Chinju*
[8]*Hanyang University, Seoul*
[9]*University of Hawaii, Honolulu, Hawaii 96822*
[10]*High Energy Accelerator Research Organization (KEK), Tsukuba*
[11]*Hiroshima Institute of Technology, Hiroshima*
[12]*University of Illinois at Urbana-Champaign, Urbana, Illinois 61801*
[13]*Institute of High Energy Physics, Chinese Academy of Sciences, Beijing*
[14]*Institute of High Energy Physics, Vienna*
[15]*Institute of High Energy Physics, Protvino*
[16]*Institute for Theoretical and Experimental Physics, Moscow*
[17]*J. Stefan Institute, Ljubljana*
[18]*Kanagawa University, Yokohama*
[19]*Korea University, Seoul*
[20]*Kyoto University, Kyoto*
[21]*Kyungpook National University, Taegu*
[22]*Swiss Federal Institute of Technology of Lausanne, EPFL, Lausanne*
[23]*University of Ljubljana, Ljubljana*
[24]*University of Maribor, Maribor*
[25]*University of Melbourne, Victoria*
[26]*Nagoya University, Nagoya*
[27]*Nara Women's University, Nara*
[28]*National Central University, Chung-li*
[29]*National United University, Miao Li*
[30]*Department of Physics, National Taiwan University, Taipei*
[31]*H. Niewodniczanski Institute of Nuclear Physics, Krakow*
[32]*Nippon Dental University, Niigata*
[33]*Niigata University, Niigata*
[34]*University of Nova Gorica, Nova Gorica*
[35]*Osaka City University, Osaka*
[36]*Osaka University, Osaka*

[37]*Panjab University, Chandigarh*
[38]*Peking University, Beijing*
[39]*University of Pittsburgh, Pittsburgh, Pennsylvania 15260*
[40]*Princeton University, Princeton, New Jersey 08544*
[41]*RIKEN BNL Research Center, Upton, New York 11973*
[42]*Saga University, Saga*
[43]*University of Science and Technology of China, Hefei*
[44]*Seoul National University, Seoul*
[45]*Shinshu University, Nagano*
[46]*Sungkyunkwan University, Suwon*
[47]*University of Sydney, Sydney NSW*
[48]*Tata Institute of Fundamental Research, Bombay*
[49]*Toho University, Funabashi*
[50]*Tohoku Gakuin University, Tagajo*
[51]*Tohoku University, Sendai*
[52]*Department of Physics, University of Tokyo, Tokyo*
[53]*Tokyo Institute of Technology, Tokyo*
[54]*Tokyo Metropolitan University, Tokyo*
[55]*Tokyo University of Agriculture and Technology, Tokyo*
[56]*Toyama National College of Maritime Technology, Toyama*
[57]*University of Tsukuba, Tsukuba*
[58]*Virginia Polytechnic Institute and State University, Blacksburg, Virginia 24061*
[59]*Yonsei University, Seoul*

(Received 2 February 2007; published 22 May 2007)

We report measurements of branching fractions and CP asymmetries for $B \to \eta K^*$ and $B \to \eta\rho$ decays. These results are obtained from a 414 fb^{-1} data sample collected at the $\Upsilon(4S)$ resonance with the Belle detector at the KEKB asymmetric-energy e^+e^- collider. We measure the following branching fractions: $\mathcal{B}(B^0 \to \eta K^{*0}) = (15.2 \pm 1.2 \pm 1.0) \times 10^{-6}$ and $\mathcal{B}(B^+ \to \eta K^{*+}) = (19.3^{+2.0}_{-1.9} \pm 1.5) \times 10^{-6}$, where the first error is statistical and the second systematic. We also find a 2.7σ excess in the $B^+ \to \eta\rho^+$ mode and measure $\mathcal{B}(B^+ \to \eta\rho^+) = (4.1^{+1.4}_{-1.3} \pm 0.4) \times 10^{-6} < 6.5 \times 10^{-6}$ at 90% confidence level. For $B^0 \to \eta\rho^0$ decays, we determine the upper limit $\mathcal{B}(B^0 \to \eta\rho^0) < 1.9 \times 10^{-6}$ at 90% confidence level. The partial rate asymmetries are $\mathcal{A}_{CP}(\eta K^{*0}) = 0.17 \pm 0.08 \pm 0.01$, $\mathcal{A}_{CP}(\eta K^{*+}) = 0.03 \pm 0.10 \pm 0.01$, and $\mathcal{A}_{CP}(\eta\rho^+) = -0.04^{+0.34}_{-0.32} \pm 0.01$.

DOI: 10.1103/PhysRevD.75.092005 PACS numbers: 13.25.Hw, 14.40.Nd

I. INTRODUCTION

Charmless hadronic B decays play an important role in understanding CP violation in the B meson system. The decays $B \to \eta K^*$ and $B \to \eta\rho$ are key examples. In the standard model (SM), penguin (tree) diagrams are expected to dominate in $B \to \eta K^*$ ($B \to \eta\rho$) decays (Fig. 1). The large branching fraction for $B \to \eta K^*$ compared to that for $B \to \eta K$ [1–3] can be explained qualitatively in terms of the interference between nonstrange and strange components of the η meson, but is higher than recent theoretical predictions [4–7]. In a similar vein, the larger measured branching fraction for charged ($B^+ \to \eta K^{*+}$) versus neutral ($B^0 \to \eta K^{*0}$) decays may suggest an additional SU(3)-singlet contribution [6–8] or constructive interference between SM penguin and tree amplitudes or between SM and new physics penguin amplitudes. Throughout this paper, the inclusion of charge-conjugate modes is implied unless stated otherwise.

In the standard model, direct CP violation (DCPV) occurs in decays due to interference between two (or more) amplitudes that have different strong and weak phases. The partial rate asymmetry can be written as

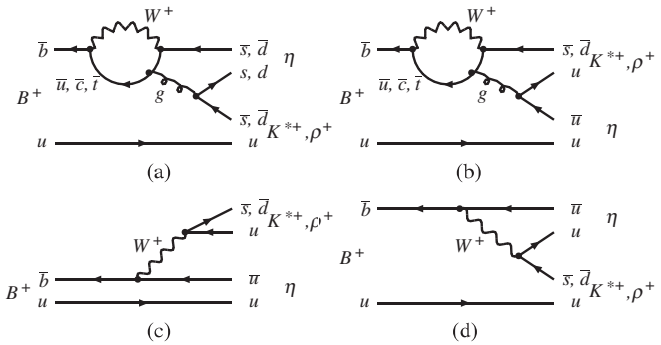

FIG. 1. Feynman diagrams for $B^+ \to \eta K^{*+}$ and $\eta\rho^+$ decays. The corresponding neutral decays are similar except that the spectator quark becomes a d and (b) and (c) diagrams do not exist.

$$\mathcal{A}_{CP}(B \to f) = \frac{\Gamma(\bar{B} \to \bar{f}) - \Gamma(B \to f)}{\Gamma(\bar{B} \to \bar{f}) + \Gamma(B \to f)} = \frac{2|M_1||M_2| \sin\Delta\delta \sin\Delta\phi}{|M_1|^2 + |M_2|^2 + 2|M_1||M_2| \cos\Delta\delta \cos\Delta\phi}, \quad (1)$$

where $\bar{B}$ and $\bar{f}$ are the CP-conjugate states, and $\Delta\delta$ ($\Delta\phi$) is the difference of the strong (weak) phases between amplitudes M_1 and M_2. Here, the amplitude M_1 (M_2) represents the sum of the amplitudes from penguin (tree) diagrams having a common weak phase. The asymmetry will be sizable when the two type of amplitudes are of comparable strength with significant phase differences. However, $B \to \eta K^*$ and $B \to \eta\rho$ decay rates are expected to be dominated by penguin diagrams for ηK^* and tree diagrams for $\eta\rho$, so $\mathcal{A}_{CP}$ is expected to be small. On the other hand, amplitudes arising from new physics may interfere with these SM amplitudes to generate a sizable $\mathcal{A}_{CP}$ value. The experimental results [3] suggest that DCPV is small, albeit with large statistical uncertainties.

II. DATA SET AND APPARATUS

This analysis is based on a data sample collected at the $\Upsilon(4S)$ resonance with the Belle detector [9] at the KEKB [10] accelerator. The data sample corresponds to an integrated luminosity of 414 fb^{-1} and contains 449×10^6 $B\bar{B}$ pairs.

The Belle detector is designed to measure charged particles and photons with high efficiency and precision. Charged-particle tracking is provided by a silicon vertex detector (SVD) and a central drift chamber (CDC) that surround the interaction region. The charged-particle acceptance covers the laboratory polar angle between $\theta = 17°$ and $150°$, measured from the z axis that is aligned antiparallel to the positron beam. Charged hadrons are distinguished by combining the responses from an array of silica aerogel Cherenkov counters (ACC), a barrel-like array of 128 time-of-flight scintillation counters (TOF), and dE/dx measurements in the CDC. The combined response provides K/π separation of at least 2.5σ for laboratory momentum up to 3.5 GeV/c. Electromagnetic showers are detected in an array of 8736 CsI(Tl) crystals (ECL) located inside the magnetic volume, which covers the same solid angle as the charged-particle tracking system. The 1.5-T magnetic field is contained via a flux return that consists of 4.7 cm thick steel plates, interleaved with resistive plate counters used for tracking muons. Two inner detector configurations were used. A 2.0 cm beampipe and a 3-layer silicon vertex detector were used for the first sample of 152×10^6 $B\bar{B}$ pairs, while a 1.5 cm beampipe, a 4-layer silicon detector and a small-cell inner drift chamber were used to record the remaining 297×10^6 $B\bar{B}$ pairs [11].

We calculate the acceptance and study backgrounds using Monte Carlo (MC) simulation. For these simulation studies, the signal events, generic $b \to c$ decays and charmless rare B decays are generated with the EVTGEN [12] event generator. The continuum MC events are generated with the $e^+e^- \to \gamma^* \to q\bar{q}$ process in the JETSET [13] generator. The GEANT3 [14] package is used for detector simulation.

III. EVENT SELECTION AND RECONSTRUCTION

Hadronic events are selected based on the charged track multiplicity and total visible energy sum, which give an efficiency greater than 99% for $B\bar{B}$ events. All primary charged tracks are required to be consistent with coming from the run-dependent interaction point within ± 2 cm along the z axis and within ± 1.5 cm in the transverse plane. Particle identification (PID) is based on the likelihoods $\mathcal{L}_K$ and $\mathcal{L}_\pi$ for charged kaons and pions, respectively. These likelihoods are calculated from CDC, TOF, and ACC information. A higher value of $\mathcal{L}_K/(\mathcal{L}_\pi + \mathcal{L}_K)$ indicates a more kaonlike particle. In this analysis, PID cuts are applied to all charged particles except those associated with $K^0_S \to \pi^+\pi^-$ decays. Unless explicitly specified, the PID cuts are $\mathcal{L}_K/(\mathcal{L}_\pi + \mathcal{L}_K) > 0.6$ for kaons and <0.4 for pions. The corresponding efficiencies are 85% for kaons and 89% for pions; 8% of pions are misidentified as kaons and 11% of kaons are misidentified as pions.

We form π^0 candidates from photon pairs with an invariant mass between 118 MeV/c^2 and 150 MeV/c^2 (2.5σ). The photon energies must exceed 50 MeV, and the π^0 momentum in the center-of-mass (CM) frame must exceed 0.35 GeV/c. K^0_S candidates are reconstructed from pairs of oppositely charged tracks whose invariant mass lies within ± 10 MeV/c^2 (2.5σ) of the K^0_S meson mass. We also require that the vertex of the K^0_S be well-reconstructed and displaced from the interaction point, and that the K^0_S momentum direction be consistent with the K^0_S flight direction.

A. η meson reconstruction

Candidate η mesons are reconstructed in the $\eta \to \gamma\gamma$ and $\eta \to \pi^+\pi^-\pi^0$ modes. If one of the photons from the former η decay mode can be paired with another photon and have a reconstructed $\gamma\gamma$ mass within 3σ of the π^0 meson mass, the η candidate is discarded. We relax the PID requirement for charged pions from the latter η decay mode to $\mathcal{L}_K/(\mathcal{L}_\pi + L_K) < 0.9$. Candidate η mesons are required to satisfy the following mass selections: 500 MeV/$c^2 \le M_{\gamma\gamma} \le$ 575 MeV/c^2 and 537 MeV/$c^2 \le M_{\pi^+\pi^-\pi^0} \le$ 557 MeV/c^2, where the reconstructed mass resolutions are 12 MeV/c^2 for $\eta \to \gamma\gamma$ and 3.5 MeV/c^2 for $\eta \to \pi^+\pi^-\pi^0$. When reconstructing the B meson candidate, the momentum of the η candidate is recalculated by applying the η mass constraint. The $\eta \to \gamma\gamma$

candidates must satisfy $|\cos\theta^*| < 0.90$, where θ^* is the angle between the photon direction and the direction of the CM frame in the η rest frame; this requirement suppresses soft photon combinatorial and $B \to K^*\gamma$ feed-across backgrounds.

B. K^* and ρ meson reconstruction

K^{*0} candidates are reconstructed from $K^+\pi^-$ and $K^0_S\pi^0$ pairs, while the K^{*+} candidates are reconstructed from $K^+\pi^0$ and $K^0_S\pi^+$ pairs. These candidates are required to have reconstructed masses within ± 75 MeV/c^2 of the nominal value [15]. Candidate ρ^0 (ρ^+) mesons are reconstructed from $\pi^-\pi^+$ ($\pi^0\pi^+$) pairs. Each combination is required to have a reconstructed mass within ± 150 MeV/c^2 of the nominal value [15].

C. B meson reconstruction

The B meson candidates are reconstructed from ηK^{*0}, ηK^{*+}, $\eta\rho^0$, and $\eta\rho^+$ combinations. They are characterized by the beam-energy-constrained mass $M_{\rm bc} = \sqrt{E^2_{\rm beam}/c^4 - |P_B/c|^2}$ and the energy difference $\Delta E = E_B - E_{\rm beam}$, where $E_{\rm beam} = 5.29$ GeV, and P_B and E_B are the momentum and energy, respectively, of the B candidate in the CM frame. We define the fit region in the $M_{\rm bc} - \Delta E$ plane as $M_{\rm bc} > 5.2$ GeV/c^2 and $|\Delta E| < 0.25$ GeV. We define the signal region as the overlap of the bands $M_{\rm bc} > 5.27$ GeV/c^2 and $|\Delta E| < 0.05$ GeV.

From signal MC, we find that 8–10% of the events contain multiple B candidates. Only one B candidate per event is retained for the likelihood fit. If there are multiple η candidates, we choose the one with the smallest χ^2 of the fit with a mass (vertex and mass) constraint to the kinematics of the η meson in the case of $\eta \to \gamma\gamma$ ($\eta \to \pi^+\pi^-\pi^0$) decays. Among the B candidates made of the same η candidate, we choose the one with the smallest vertex χ^2 in the cases of $K^{*0} \to K^+\pi^-$ or $\rho^0 \to \pi^+\pi^-$; or then the one with the mass closest to nominal in the case of $K^{*+} \to K^0\pi^+$; or then the π^0 mass closest to the nominal in all other cases.

IV. BACKGROUND SUPPRESSION

The dominant background for exclusive two-body B decays comes from the $e^+e^- \to \gamma^* \to q\bar{q}$ continuum ($q = u, d, s, c$), which has a jetlike event topology in contrast to more spherical $B\bar{B}$ events. The other major backgrounds involve feed-across from these and other charmless B decays. The background from $b \to c$ decays has a small impact because the $M_{\rm bc}$ and ΔE distributions do not peak in the signal region. In this analysis, the fit does not distinguish nonresonant $B \to \eta K\pi$ decays from $B \to \eta K^*$ decays, since they have the same $M_{\rm bc}$ and ΔE distributions. The nonresonant contribution is estimated and subtracted independently using the $K\pi$ invariant mass distributions of the fitted B-decay yields.

A. Continuum background

Signal and continuum events are distinguished in two steps. Here, all the variables are calculated in the CM frame. First, we require $|\cos\theta_T| < 0.9$, where θ_T is defined as the angle between the η direction of a B candidate and the thrust axis from all particles in the event not associated with that B candidate. This retains 90% of signal and removes ~56% of continuum. Second, a likelihood $\mathcal{L}_s$ ($\mathcal{L}_c$) for signal (continuum) is formed from two independent variables—$\cos\theta_B$, where θ_B is the polar angle of the B candidate momentum direction, and a Fisher discriminant [16] $\mathcal{F} = \vec{\alpha} \cdot \vec{R}$ that combines seven event shape variables: $\cos\theta_T$, $S_\perp$ (the sum of the magnitudes of the momenta transverse to the η direction for all particles more than 45° away from the η axis, divided by the sum of the magnitudes of the momenta of all particles not from the candidate B meson [17]), and the five modified Fox-Wolfram moments [18] R^{so}_2, R^{so}_4, R^{oo}_2, R^{oo}_3, and R^{oo}_4. The Fisher discriminant's weight vector $\vec{\alpha}$ is determined to maximize the separation between signal events and continuum background using MC data; these Fox-Wolfram moments are used since they are not correlated with $M_{\rm bc}$. The likelihood ratio $\mathcal{R} = \mathcal{L}_s/(\mathcal{L}_s + \mathcal{L}_c)$, which peaks near one for signal and near zero for continuum, is used to distinguish signal from continuum.

The distribution of $\mathcal{R}$ is found to depend somewhat on the event's B flavor tagging quality parameter r [19], which ranges from zero for no flavor identification to unity for unambiguous flavor assignment. We partition the data into three r regions, $r \le 0.5$, $0.5 < r \le 0.75$, and $r > 0.75$. In each r region, the optimal cut on $\mathcal{R}$ is determined by maximizing the significance $N_S/\sqrt{N_S + N_B}$, where N_S and N_B are the retained number of signal and continuum-background events selected in MC samples. For cut optimization studies, we assume the branching fractions of 2.0×10^{-5} for ηK^*, 5.0×10^{-6} for $\eta\rho^+$, and 1.0×10^{-6} for $\eta\rho^0$. For $B^0 \to \eta K^{*0}$, $\eta \to \gamma\gamma$, $K^{*0} \to K^+\pi^-$ decays, a typical cut of $\mathcal{R} > 0.4$ is ~87% efficient for signal and removes ~67% of the continuum background for data in the region $r \le 0.5$, and a cut of $\mathcal{R} > 0.2$ is ~94% efficient for signal and removes ~53% of the continuum background for data in the region $r > 0.75$.

B. Backgrounds from B decays

$B \to K^*(\rho)\gamma$ is the dominant charmless B-decay background for $B \to \eta K^*(\rho)$, $\eta \to \gamma\gamma$ decays. The $\eta \to \gamma\gamma$ selection, $|\cos\theta^*| < 0.90$, removes 85% of this background. To further suppress it, we pair each photon from the $\eta \to \gamma\gamma$ candidate with the K^* or ρ candidate and reject those events where $M_{\rm bc} > 5.27$ GeV/c^2 and -0.2 GeV $< \Delta E < 0.1$ GeV. We thus remove 96% of this background and retain 93% of the signal events. For $B \to \eta\rho$ decays, a measurable contribution from other charmless B and $b \to c$ decays remains (see Table I).

TABLE I. Estimated B-decay background contributions in the fit region to $B \to \eta\rho$ from $b \to c$ ($N_{\rm bc}$), charmless B decay ($N_{\rm r}$), and ηK^* feed-across ($N_{\rm feed}$) and measured yields from all sources (N) but dominated by residual continuum background, after application of the $\cos\theta_T$ and $\mathcal{R}$ cuts. $N_{\rm bc}$ and $N_{\rm r}$ are estimated from MC samples.

Mode	$N_{\rm bc}$	$N_{\rm r}$	$N_{\rm feed}$	N
$\eta_{\gamma\gamma}\rho^0$	62	81	17	2931
$\eta_{\pi\pi\pi^0}\rho^0$	67	27	5	1063
$\eta_{\gamma\gamma}\rho^+$	148	74	3	4169
$\eta_{\pi\pi\pi^0}\rho^+$	76	22	1	1809

The contributions of these backgrounds are taken into account in the analysis.

V. ANALYSIS PROCEDURE

Signal yields are obtained using an extended unbinned maximum likelihood fit to the $M_{\rm bc}$ and ΔE distributions (2D ML) for events that satisfy the $\cos\theta_T$ and $\mathcal{R}$ requirements.

For N input candidates, the likelihood is defined as

$$L = \frac{e^{-(N_S+N_{qq}+N_{\rm bc}+N_{\rm r}+N_{\rm feed})}}{N!}\prod_{i=1}^{N}(N_S P_{S_i} + N_{qq}P_{qq_i} + N_{\rm bc}P_{{\rm bc}_i} + N_{\rm r}P_{{\rm r}_i} + N_{\rm feed}P_{{\rm feed}_i}), \quad (2)$$

where P_{S_i}, P_{qq_i}, $P_{{\rm bc}_i}$, $P_{{\rm r}_i}$, and $P_{{\rm feed}_i}$ are the probability density functions for event i, with measured values $M_{{\rm bc},i}$ and ΔE_i, to arise from signal, continuum background, $b \to c$ background, charmless B decay background, and feed-across background, respectively. The small yields $N_{\rm bc}$, $N_{\rm r}$, and $N_{\rm feed}$ are fixed from the MC analysis.

The continuum, $b \to c$ and charmless B-decay background ΔE probability density functions (PDF) are modeled by second- or third-order polynomial functions. The continuum and $b \to c$ background components in $M_{\rm bc}$ are modeled by a smooth function [20]. To account for the peaking behavior of $M_{\rm bc}$ in the signal region from charmless B decay backgrounds, we use the sum of two bifurcated-Gaussian functions to model the distributions. The bifurcated Gaussian combines the left half of a wide-resolution Gaussian with the right half of a narrow-resolution Gaussian, both having a common mean. For $B \to \eta\rho$ decays, the $M_{\rm bc}$ and ΔE distributions from ηK^* feed-across will behave like signal with a ΔE shift of -50 MeV. The PDF shape for each contribution is determined from MC. The first-order coefficient of the continuum-background ΔE polynomial and the parameters of the $M_{\rm bc}$ function are allowed to float in each fit.

For the signal ΔE distribution, we combine two bifurcated-Gaussian functions. The first accounts for 60–80% of the total area and the wider second models the low-energy tail. $M_{\rm bc}$ is weakly correlated with ΔE, so we construct separate bifurcated Gaussians for $M_{\rm bc}$ in the three ranges $|\Delta E| < 0.05$ GeV, $0.05\ {\rm GeV} < |\Delta E| < 0.1$ GeV, and $0.1\ {\rm GeV} < |\Delta E| < 0.25$ GeV. The parameters of these functions are estimated from MC first, then calibrated with a large control sample of $B^+ \to D^0\pi^+$, $D^0 \to K^+\pi^-\pi^0$ decays.

For decays with more than one subdecay process, the final results are obtained by fitting the subdecay modes simultaneously with the expected efficiencies folded in and with the branching fraction as the common output. The statistical significance (Σ) of the signal is defined as $\sqrt{-2\ln(L_0/L_{\rm max})}$, where L_0 and $L_{\rm max}$ denote the likelihood values for zero signal events and the best fit numbers, respectively.

The 90% confidence level (C.L.) upper limit x_{90} on the signal yield is calculated from the equation

$$\frac{\int_0^{x_{90}} L(x)dx}{\int_0^{\infty} L(x)dx} = 90\%.$$

To incorporate the systematic uncertainty in the calculation of x_{90}, the likelihood function is smeared with a Gaussian function with the resolution from the systematic uncertainty. That smeared likelihood function is also used to calculate the significance of the signal including the systematic uncertainty.

VI. MEASUREMENTS OF BRANCHING FRACTIONS

A. Efficiencies and corrections

The overall reconstruction efficiency ϵ is first obtained using MC samples and then multiplied by PID efficiency corrections obtained from data. The PID efficiency correction is determined using $D^{*+} \to D^0\pi^+$, $D^0 \to K^-\pi^+$ data samples. Other MC efficiency corrections are determined by comparing data and MC predictions for other well-known processes. The charged-particle tracking efficiency correction is studied using a high-momentum η sample and is determined by comparing the ratios of $\eta \to \pi^+\pi^-\pi^0$ to $\eta \to \gamma\gamma$ in data and MC. The same high-momentum η sample is also used for π^0 reconstruction efficiency corrections by comparing the ratio of $\eta \to \pi^0\pi^0\pi^0$ to $\eta \to \gamma\gamma$ between the data and MC sample. The K^0_S reconstruction efficiency is verified by comparing four $K^*(892)$ decay channels ($K^+\pi^-$, $K^+\pi^0$, $K^0_S\pi^+$, $K^0_S\pi^0$) in inclusive K^* and exclusive $B \to J/\psi K^*$ samples. The $\mathcal{R}$ cut efficiency correction is determined using $B^+ \to \bar{D}^0\pi^+$ decays. For η and K^* reconstruction and mass cuts, we use the high-momentum η and K^* sample for the efficiency correction studies. The above studies show good agreement between data and MC; the reconstruction and selection efficiencies differ by about 2%. The PID, π^0, η, and K^* reconstruction efficiency corrections are applied and the systematic uncertainties are also obtained from the above studies.

TABLE II. Summary of results for each channel listed in the first column. The measured signal yield (N_S), reconstruction efficiency (ϵ), total efficiency ($\epsilon_{\rm tot}$) including the secondary branching fraction, statistical significance (Σ) and measured branching fractions are shown. Uncertainties shown in second and sixth columns are statistical only. For the final combined branching fractions, corrections for contributions from nonresonant or higher resonance components have been applied. The total systematic uncertainties are given, and the combined significances include the systematic uncertainties.

Mode	N_S	ϵ (%)	$\epsilon_{\rm tot}$ (%)	Σ	$\mathcal{B}(10^{-6})$
$\eta_{\gamma\gamma}K^{*0}_{K^+\pi^-}$	$336.2^{+30.1}_{-29.2}$	16.9	4.4	14.2	16.9 ± 1.5
$\eta_{\pi\pi\pi^0}K^{*0}_{K^+\pi^-}$	$93.4^{+14.6}_{-13.8}$	9.8	1.5	8.7	$14.1^{+2.2}_{-2.1}$
$\eta_{\gamma\gamma}K^{*0}_{K^0\pi^0}$	$20.1^{+7.5}_{-6.7}$	2.1	0.27	3.6	$16.7^{+6.3}_{-5.6}$
$\eta_{\pi\pi\pi^0}K^{*0}_{K^0\pi^0}$	$9.5^{+5.0}_{-4.2}$	1.3	0.098	2.6	$21.6^{+11.5}_{-9.7}$
ηK^{*0}	...	...	...	15.7	$15.2 \pm 1.2 \pm 1.0$
$\eta_{\gamma\gamma}K^{*+}_{K^+\pi^0}$	$79.8^{+16.1}_{-15.3}$	6.7	0.88	6.1	$20.1^{+4.1}_{-3.9}$
$\eta_{\pi\pi\pi^0}K^{*+}_{K^+\pi^0}$	$24.1^{+8.7}_{-7.9}$	4.2	0.32	3.5	$16.9^{+6.1}_{-5.6}$
$\eta_{\gamma\gamma}K^{*+}_{K^0\pi^+}$	$120.3^{+16.2}_{-15.4}$	4.5	1.2	10.1	$22.6^{+3.1}_{-2.9}$
$\eta_{\pi\pi\pi^0}K^{*+}_{K^0\pi^+}$	$29.2^{+7.3}_{-6.6}$	2.6	0.38	6.2	$16.9^{+4.3}_{-3.8}$
ηK^{*+}	...	...	...	12.3	$19.3^{+2.0}_{-1.9} \pm 1.5$
$\eta_{\gamma\gamma}\rho^0$	$19.5^{+11.3}_{-10.4}$	8.9	3.5	2.1	$1.25^{+0.73}_{-0.67}$
$\eta_{\pi\pi\pi^0}\rho^0$	$0.9^{+4.6}_{-3.9}$	5.5	1.2	0.2	$0.17^{+0.84}_{-0.66}$
$\eta\rho^0$	...	...	...	1.3	$0.84^{+0.56}_{-0.51} \pm 0.19$
$\eta_{\gamma\gamma}\rho^+$	$38.1^{+16.1}_{-15.2}$	5.5	2.2	2.6	$3.9^{+1.7}_{-1.6}$
$\eta_{\pi\pi\pi^0}\rho^+$	$15.8^{+8.9}_{-8.0}$	3.50	0.79	2.1	$4.4^{+2.5}_{-2.2}$
$\eta\rho^+$	...	...	...	2.7	$4.1^{+1.4}_{-1.3} \pm 0.4$

B. Fit results

The fitted signal yields and branching fractions are shown in Table II. Several consistency checks are made, including tighter $\mathcal{R}$ cuts as well as 1D ML $M_{\rm bc}$ and ΔE fits, and they are all found to be consistent. The total observed yields are $N_{\eta K^{*0}} = 459.2^{+34.6}_{-33.3}$ for $B^0 \to \eta K^{*0}$, $N_{\eta K^{*+}} = 253.4^{+25.5}_{-24.0}$ for $B^+ \to \eta K^{*+}$, $N_{\eta\rho^0} = 20.4^{+12.2}_{-11.0}$ for $B^0 \to \eta\rho^0$ and $N_{\eta\rho^+} = 53.9^{+18.4}_{-17.1}$ for $B^+ \to \eta\rho^+$. Figure 2 shows the projections of the data and the fits onto $M_{\rm bc}$ (for events in ΔE signal slice) and ΔE (for events in the $M_{\rm bc}$ signal slice) for the $B \to \eta K^*$ decays, while Fig. 3 shows the corresponding projections for the $B \to \eta\rho$ decays.

C. Non $K^*(892)$ components

The background-subtracted K^* helicity distributions within the $M_{\rm bc}$ and ΔE signal regions (Fig. 4) are consistent with the expectation from ηK^* decays, indicating no significant S-wave or higher resonance contribution in the K^* mass region. The $K^{*0}(K^{*+})$ helicity angle ($\theta_{\rm hel}$) is the angle between the $\pi^-(\pi^0, K^0)$ direction and the opposite of the B direction in the K^* rest frame. The binned χ^2 per degree of freedom is $\chi^2/N = 9.7/10$ for K^{*0} and $\chi^2/N = 3.6/10$ for K^{*+}.

We use a 2D-ML fit to the $K\pi$ invariant mass distributions to evaluate the small S-wave or higher resonance $K\pi$ contaminations in the K^* mass region. A clear excess in the higher $K\pi$ invariant mass region is observed (Fig. 5). To estimate these contributions, we fit the distributions with a P-wave relativistic Breit-Wigner function for the $K^*(892)$, a D-wave relativistic Breit-Wigner function for the $K_2^*(1430)$ resonance and an *ad hoc* function for the S-wave contribution. Several functions are used to model the S-wave contribution in the $K\pi$ mass region 1.0 GeV/c^2 to 1.5 GeV/c^2, including a $K_0^*(1350)$ resonance [21], the LASS distribution [21], and a threshold function. The LASS distribution contains a nonresonant S-wave background function interfering with an S-wave $K_0^*(1430)$ resonance. Figure 5 shows one example of our fitting results with the S-wave contribution modeled by the LASS distribution. Based on these studies with various S-wave functions, the nonresonant $K\pi$ contributions are $(5.6 \pm 3.0)\%$ for ηK^{*0} and $(5.0 \pm 3.0)\%$ for ηK^{*+} decays. These corrections are applied to the final branching fraction measurements of $B \to \eta K^*$.

For $B^+ \to \eta\rho^+$ decays, we examine the properties of the ρ^+ candidates through 2D ML fits in bins of $\pi^+\pi^0$ invariant mass and ρ^+ helicity. Although statistically limited, a ρ^+ mass peak and a polarized ρ^+ helicity distribu-

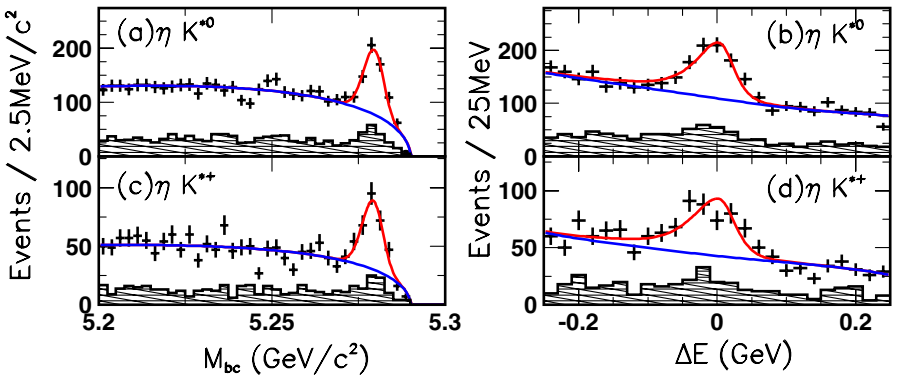

FIG. 2 (color online). Projections on $M_{\rm bc}$ (for the signal slice in ΔE) and ΔE (for the signal slice in $M_{\rm bc}$) for ηK^{*0} (a,b) and ηK^{*+} (c,d) with the expected signal and background curves overlaid. The shaded area represents $\eta \to \pi^+\pi^-\pi^0$ decays.

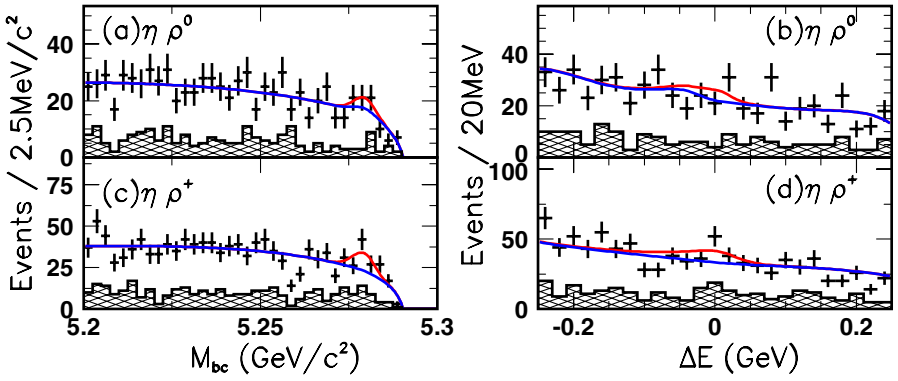

FIG. 3 (color online). Projections on M_{bc} (for the signal slice in ΔE) and ΔE (for the signal slice in $M_{\rm bc}$) from 2D ML fit results for $\eta\rho^0$ (a,b) and $\eta\rho^+$ (c,d) with the expected signal and background curves overlaid. The shaded area represents $\eta \to \pi^+\pi^-\pi^0$ decays.

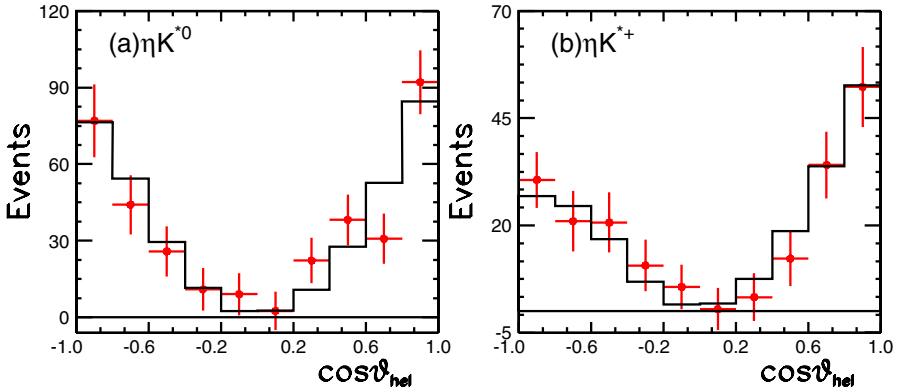

FIG. 4 (color online). Distributions of the K^* helicity for the (a) K^{*0} and (b) K^{*+} modes in case of $B \to \eta K^*$ decays. The overlaid histograms represent the distributions from MC normalized by the 2D fit results.

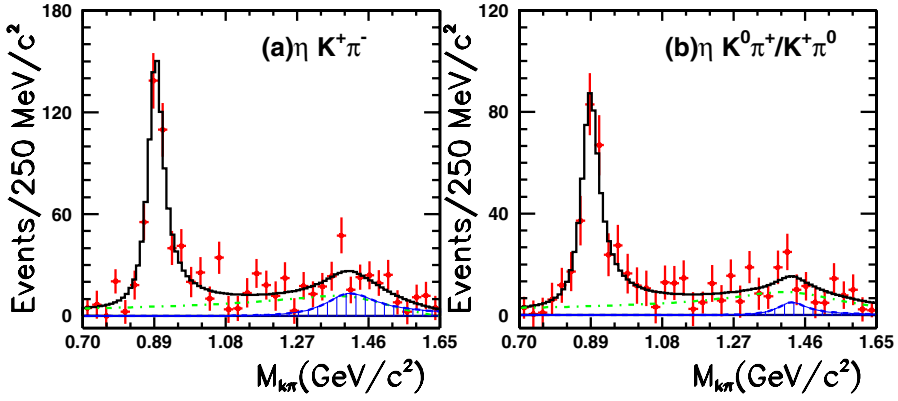

FIG. 5 (color online). Fitted yields vs the $K\pi$ invariant mass for the (a) $(K\pi)^0$ and (b) $(K\pi)^+$ modes. The overlaid functions are the results of a binned χ^2 fit. The dashed line represents the contribution from the D-wave $K_2^*(1430)$, and the dashed-dotted line represents the LASS S-wave parameterization. LASS parameterization parameters, widths of P-wave and D-wave functions are allowed to float in the fits.

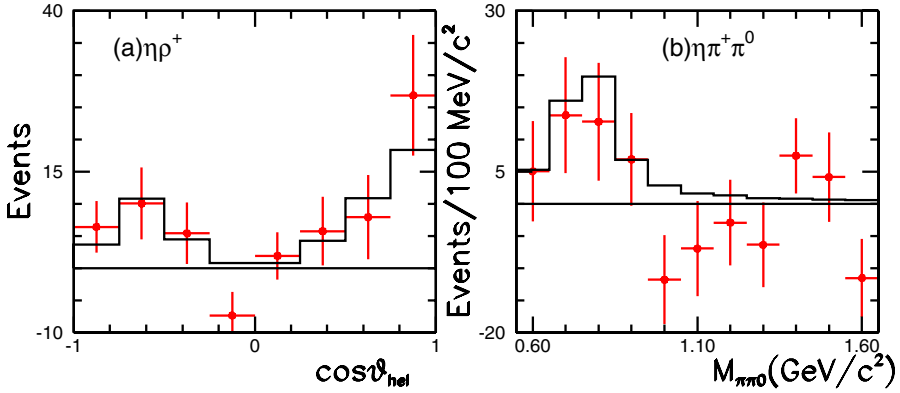

FIG. 6 (color online). Fitted yields vs (a) ρ^+ helicity and (b) $\pi^+\pi^0$ invariant mass from $B \to \eta\rho^+$ decays. The overlaid histograms are expected distributions from MC and normalized by the 2-D fit results with $\chi^2/N = 6.8/8$ for (a) and $\chi^2/N = 13.6/11$ for (b).

tion are observed (Fig. 6) and are consistent with the expectation from $\eta\rho^+$. Because of the limited statistics for $B^+ \to \eta\rho^+$ decays, a larger systematic error for the nonresonant or higher resonance contributions is assigned with no corrections applied.

VII. SYSTEMATIC ERROR

Systematic errors, enumerated in Table III, arise from efficiency corrections, nonresonant corrections and fitting. The main sources of uncertainties in the efficiency corrections are from the reconstruction of low-momentum charged tracks, low-energy photon finding, and the $\mathcal{R}$ cut efficiency. The systematic errors include contributions of 1% for $\mathcal{R}$ cuts, 1% per reconstructed charged particle, 0.5% for each charged-particle identification, 4% for π^0 reconstruction, 4.5% for K^0_S reconstruction, and 2% for η reconstruction with $\eta \to \gamma\gamma$. We use $B^+ \to D^0\pi^+$ decays to estimate the uncertainties in the signal PDF's used for fitting $M_{\rm bc}$ and ΔE by comparing the mean and the width of the $M_{\rm bc}$ and ΔE distributions between the $B^+ \to D^0\pi^+$ data and the MC sample. In Table III, "Fit" means the systematic uncertainty from the PDF function modeling. "B_s" means the systematic uncertainty from the braching fractions of η and $K^*(\rho)$ decays, which is obtained from the PDG tables [15]. "Nonresonant" means the systematic uncertainty from the nonresonant or higher resonant contributions in the $K^*(\rho)$ mass window regions, which is obtained from the studies of a 2D-ML fit to the $K\pi$ invariant mass distribution. For MC estimated $b \to c$ and charmless B decay backgrounds ("$N_{\rm bc}$" and "$N_{\rm r}$," respectively), we vary the estimated yields by $\pm 50\%$ and refit the data. The difference between the resulting signal yield and the nominal value is taken as an additional systematic error. The overall relative systematic errors are 6.5% for ηK^{*0}, 7.5% for ηK^{*+}, 22.1% for $\eta\rho^0$ and 9.6% for $\eta\rho^+$.

TABLE III. Relative systematic errors for ηK^* and $\eta\rho$. The unit is in percent (%).

Contribution	ηK^{*0}	ηK^{*+}	$\eta\rho^0$	$\eta\rho^+$
Charged track/K^0_S reconstruction	2.9	4.4	3.3	1.8
$\pi^0/\eta \to \gamma\gamma$ selection	2.8	3.5	3.2	4.8
η mass window	2.0	2.0	2.0	2.0
$K^*(\rho)$ mass window	2.0	2.0	2.0	2.0
PID correction	1.3	1.0	1.6	0.8
$\mathcal{R}$ requirement	1.0	1.0	1.0	1.0
Fit	1.7	1.8	7.5	4.2
$N_{\rm bc}$, $N_{\rm r}$	1.2	1.2	7.5	0.4
ηK^* feed-across	...	...	17.4	1.1
$N_{B\bar{B}}$	1	1	1	1
B_s	1.0	1.0	1.4	0.8
Nonresonant	3.0	3.0	6.0	6.0
Total	6.5	7.5	22.1	9.6

VIII. $\mathcal{A}_{CP}$ MEASUREMENTS

We measure $\mathcal{A}_{CP}$ for $B \to \eta K^*$ and $B^+ \to \eta\rho^+$. To account for the wrong-tag fraction w, the true value of $\mathcal{A}_{CP}$ is related to the measured $\mathcal{A}^{\rm obs}_{CP}$ via $\mathcal{A}^{\rm obs}_{CP} = (1 - 2w)\mathcal{A}_{CP}$. Among the decay modes we study, only those in which the $\mathcal{A}_{CP}$ values are determined by low-momentum charged pions have a significant w: the wrong-tag fractions for $K^{*+} \to K^0\pi^+$ is $\sim 1.5\%$ for ηK^{*+} decays and $\sim 2.0\%$ for $\eta\rho^+$ decays, while other decays have $w < 0.1\%$. Since the result for ηK^{*+} is obtained from a simultaneous fit to all four subdecay modes with roughly equal statistics for $K^{*+} \to K^+\pi^0$ and $K^{*+} \to K^0\pi^+$, the wrong-tag effect for $\mathcal{A}_{CP}$ is less than 0.7%. Therefore, the only mode where we apply a correction due to the wrong-tag fraction is $B^+ \to \eta\rho^+$, where we estimate $w = 2\%$. To incorporate the CP asymmetry in the fit, the coefficients of the signal and continuum-background PDF's in the likelihood are modified as follows: $N_S \to \frac{1}{2}N_S(1 - q\mathcal{A}^{\rm obs}_{CP})$ and $N_{qq} \to \frac{1}{2}N_{qq}(1 - q\mathcal{A}_{CP,qq})$, where $q = +1(-1)$ for a $B(\bar{B})$ meson tag and $\mathcal{A}^{\rm obs}_{CP}$, $\mathcal{A}_{CP,qq}$ are the $\mathcal{A}_{CP}$ outputs for signal and continuum, respectively. The results are $\mathcal{A}^{\rm obs}_{CP}(\eta K^{*0}) = 0.17 \pm 0.08$, $\mathcal{A}^{\rm obs}_{CP}(\eta K^{*+}) = 0.03 \pm 0.10$, and $\mathcal{A}^{\rm obs}_{CP}(\eta\rho^+) = -0.04^{+0.34}_{-0.32}$.

Since the systematic errors in the reconstruction of the η candidates and the number of $B\bar{B}$ events cancel in the ratio, the systematic uncertainty on $\mathcal{A}_{\mathcal{CP}}$ comes mainly from the charge asymmetry in the identification of charged kaons and the fitting PDF's. To estimated the fitting-PDF systematic uncertainty, we apply the same procedures as in the branching fraction measurements. The relative systematic errors from fitting PDF's are estimated to be 3% for ηK^{*0}, 13% for ηK^{*+}, and 27% for $\eta\rho^+$. The efficiency asymmetry for the PID of charged kaons is 0.01 in absolute value.

IX. SUMMARY

In summary, we report measurements of the exclusive two-body charmless hadronic $B \to \eta K^*$ and $B \to \eta\rho$ decays with high statistics. Our results are consistent with previous measurements [1,3] and confirm that the branching fractions for $B^0 \to \eta K^{*0}$ and $B^+ \to \eta K^{*+}$ are large. The branching fractions obtained are $\mathcal{B}(B^0 \to \eta K^{*0}) = (15.2 \pm 1.2 \pm 1.0) \times 10^{-6}$, and $\mathcal{B}(B^+ \to \eta K^{*+}) = (19.3^{+2.0}_{-1.9} \pm 1.5) \times 10^{-6}$, where the first error is statistical and the second systematic. Our measurements indicate that the branching fraction for $B^+ \to \eta K^{*+}$ is 1.4σ higher than that for $B^0 \to \eta K^{*0}$. A 2.7σ excess is seen for $B^+ \to \eta\rho^+$ decays. The branching fraction and 90% C.L. upper limits for $B \to \eta\rho$ decays are $\mathcal{B}(B^+ \to \eta\rho^+) = (4.1^{+1.4}_{-1.3} \pm 0.4) \times 10^{-6} (< 6.5 \times 10^{-6})$ and $\mathcal{B}(B^0 \to \eta\rho^0) < 1.9 \times 10^{-6}$. The measurements of the $B \to \eta\rho$ branching fractions are consistent with theoretical predictions [4–7].

We have measured the direct CP asymmetry in the $B \to \eta K^*$ and $B^+ \to \eta\rho^+$ channels. Our results are $\mathcal{A}_{CP}(\eta K^{*0}) = 0.17 \pm 0.08 \pm 0.01$, $\mathcal{A}_{CP}(\eta K^{*+}) = 0.03 \pm 0.10 \pm 0.01$, and $\mathcal{A}_{CP}(\eta\rho^+) = -0.04^{+0.34}_{-0.32} \pm 0.01$, all consistent with no asymmetry.

ACKNOWLEDGMENTS

We thank the KEKB group for the excellent operation of the accelerator, the KEK cryogenics group for the efficient operation of the solenoid, and the KEK computer group and the National Institute of Informatics for valuable computing and Super-SINET network support. We acknowledge support from the Ministry of Education, Culture, Sports, Science, and Technology of Japan and the Japan Society for the Promotion of Science; the Australian Research Council and the Australian Department of Education, Science and Training; the National Science Foundation of China and the Knowledge Innovation Program of the Chinese Academy of Sciences under Contract Nos. 10575109 and IHEP-U-503; the Department of Science and Technology of India; the BK21 program of the Ministry of Education of Korea, the CHEP SRC program and Basic Research program (Grant No. R01-2005-000-10089-0) of the Korea Science and Engineering Foundation, and the Pure Basic Research Group program of the Korea Research Foundation; the Polish State Committee for Scientific Research; the Ministry of Education and Science of the Russian Federation and the Russian Federal Agency for Atomic Energy; the Slovenian Research Agency; the Swiss National Science Foundation; the National Science Council and the Ministry of Education of Taiwan; and the U.S. Department of Energy.

[1] B. H. Behrens *et al.* (CLEO Collaboration), Phys. Rev. Lett. **80**, 3710 (1998); S. J. Richichi *et al.*, Phys. Rev. Lett. **85**, 520 (2000).
[2] P. Chang *et al.* (Belle Collaboration), Phys. Rev. D **71**, 091106(R) (2005).
[3] B. Aubert *et al.* (BABAR Collaboration), Phys. Rev. Lett. **95**, 131803 (2005); B. Aubert *et al.*, Phys. Rev. Lett. **97**, 201802 (2006).
[4] A. Ali, G. Kramer, and C.-D. Lu, Phys. Rev. D **58**, 094009 (1998); Xin Liu, Huisheng Wang, Zhenjun Xiao, Libo Guo, and C.-D. Lu, Phys. Rev. D **73**, 074002 (2006).
[5] Y.-H. Chen, H.-Y. Cheng, B. Tseng, and K.-C. Yang, Phys. Rev. D **60**, 094014 (1999); H.-Y. Cheng and K. C. Yang, Phys. Rev. D **62**, 054029 (2000).
[6] M.-Z. Yang and Y. D. Yang, Nucl. Phys. **B609**, 469 (2001); M. Beneke and M. Neubert, Nucl. Phys. **B651**, 225 (2003); D. Du, H. Gong, J. Sun, D. Yang, and G. Zhu, Phys. Rev. D **65**, 094025 (2002).
[7] M. Gronau and J. L. Rosner, Phys. Rev. D **61**, 073008 (2000); C.-W. Chiang and J. L. Rosner, Phys. Rev. D **65**, 074035 (2002); C.-W. Chiang, M. Gronau, Z. Luo, J. L. Rosner, and D. A. Suprun, Phys. Rev. D **69**, 034001 (2004).
[8] W.-S. Hou and K.-C. Yang, Phys. Rev. D **61**, 073014 (2000).
[9] K. Abashian *et al.* (Belle Collaboration), Nucl. Instrum. Methods Phys. Res., Sect. A **479**, 117 (2002).
[10] S. Kurokawa and E. Kikutani, Nucl. Instrum. Methods Phys. Res., Sect. A **499**, 1 (2003), and other papers therein.
[11] Z. Natkaniec *et al.* (Belle SVD2 Group), Nucl. Instrum. Methods Phys. Res., Sect. A **560**, 1 (2006).
[12] D. J. Lange, Nucl. Instrum. Methods Phys. Res., Sect. A **462**, 152 (2001).
[13] T. Sjöstrand, Comput. Phys. Commun. **82**, 74 (1994); T. Sjöstrand and M. Bengston, Comput. Phys. Commun. **43**, 367 (1987); T. Sjöstrand, Comput. Phys. Commun. **39**, 347 (1986).
[14] R. Brun *et al.*, GEANT 3.21, CERN Report No. DD/EE/84-1, 1984.
[15] S. Eidelman *et al.* (Particle Data Group), Phys. Lett. B

592, 1 (2004).
[16] R. A. Fisher, Annals Eugenics **7**, 179 (1936).
[17] R. Ammar *et al.* (CLEO Collaboration), Phys. Rev. Lett. **71**, 674 (1993).
[18] The Fox-Wolfram moments were introduced in G. C. Fox and S. Wolfram, Phys. Rev. Lett. **41**, 1581 (1978). The modified Fox-Wolfram moments used in this paper is described in C. H. Wang *et al.* (Belle Collaboration), Phys. Rev. D **70**, 012001 (2004).
[19] H. Kakuno *et al.*, Nucl. Instrum. Methods Phys. Res., Sect. A **533**, 516 (2004).
[20] H. Albrecht *et al.*, Phys. Lett. B **241**, 278 (1990).
[21] D. Aston *et al.* (LASS Collaboration), Nucl. Phys. **B296**, 493 (1988).